To be published in Nuclear Instruments and Methods (A) SRF041014-03

Dynamical Aspects of Multipacting Induced Discharge in a Rectangular Waveguide

R.L. Geng [a,*], P. Goudket [b], R.G. Carter [c], S. Belomestnykh [a], H. Padamsee [a], D.M. Dykes [b]

[a] *Laboratory for Elementary Particle Physics, Cornell University, Ithaca, NY14853, USA*

[b] *ASTeC, CLRC Daresbury Laboratory, Warrington WA4 4AD, UK*

[c] *Engineering Department, Lancaster University, Lancaster LA1 4YR, UK*

Abstract

Multipacting induced discharge in a rectangular waveguide is studied experimentally at a RF frequency of 500 MHz. The waveguide has a cross-section of 457 mm by 102 mm. The maximum forward RF power is 600 kW and 300 kW in traveling and standing wave mode respectively. A continuous multipacting band structure is observed. Electron pick-up probes of antenna-type are used to measure the multipacting current and its longitudinal as well as horizontal distributions. The electron energy spectrum is measured with the retarding field method. The end-point energy of the spectra taken in traveling wave mode is in the range of 100-1000 eV and agrees well with the impact energy calculated by the classical multipacting theory. However, a large fraction of electrons has energies lower than 100 eV. Electron stimulated gas desorption is found to play a critical role in the dynamics of multipacting induced breakdown. It is concluded that the ionization discharge of desorbed gases is the immediate cause for RF breakdown.

Key words: Multipacting, Rectangular waveguide, Electron impact energy, Discharge, Electron stimulated desorption
PACS: 84.40.Az, 52.80.Vp, 52.80.Pi, 79.20.La, 79.20.Hx

* Corresponding author.
Email address: rg58@cornell.edu (R.L. Geng).

1 Introduction

Multipacting induced breakdown in rectangular waveguides as well as in coaxial lines is among the leading mechanisms impeding smooth operation of high power RF couplers for RF cavities in modern accelerators for colliding beam physics and synchrotron radiation facilities. A hard multipacting barrier can even represents a power limit in some cases. As the power demand continues to increase for both pulsed and CW operations of RF couplers, the studies of this mechanism have received renewed interests recently [1]-[4].

There are various types of multipacting depending on the geometry of the RF structure and the configuration of the RF field. Two-sided multipacting is of primary concern in the context of the present studies. The theory of two-sided multipacting in a parallel-plate was developed by Gill and von Engel [5]. Hatch and Williams extended the work and introduced what is now called Hatch diagram, which gives the multipacting susceptible zones in a graph of the RF voltage plotted against the frequency-gap product [6]. The experimentally measured minimum breakdown voltage was found to be in good agreement with the envelope of Hatch diagram [6][7]. The applicability of Hatch diagram to rectangular waveguide geometry was evaluated also experimentally and the results are fairly satisfactory [8]. Fig. 1 shows a Hatch diagram reproduced from Ref. [6]. It depicts the first five theoretical multipacting zones, together with some experimental data obtained from parallel-plates and RF cavities. Measurement results from rectangular waveguides made of aluminum [8] are also shown in Fig. 1.

It has been customary for RF designers to use Hatch diagram as a guide to avoid multipacting when building practical RF structures. However, for the following reasons, the applicability of Hatch diagram to rectangular waveguides used in RF couplers for today's modern accelerators has limitation. First of all, the present work primarily deals with higher order (the order is defined as the transit time between the two successive impacts in units of the half-period of the RF) multipacting, which was first observed in the rectangular waveguide coupler of the CESR superconducting RF system [12] and later elaborated in Ref. [3]. The dominant multipacting modes of current concern are higher order ones with a large order number N of ≥ 9. Unfortunately, experimental verification of Hatch diagram with regard to higher order multipacting has been scarce (Fig. 1). More importantly, smooth operation of a waveguide coupler relies on the proper choice of a safe working point, that is away from a "hard" multipacting barrier [1]. But a Hatch diagram provides little information about

[1] A hard barrier is one that can not be eliminated by RF processing. The hardness of a multipacting barrier is closely related to the electron impact energy. A practical rule is in authors' opinion that a hard barrier has an impact energy of $>E_{max}$, where E_{max} is the impact energy at which SEY reaches its maximum. Typical E_{max} is in the range of 300-400 eV.

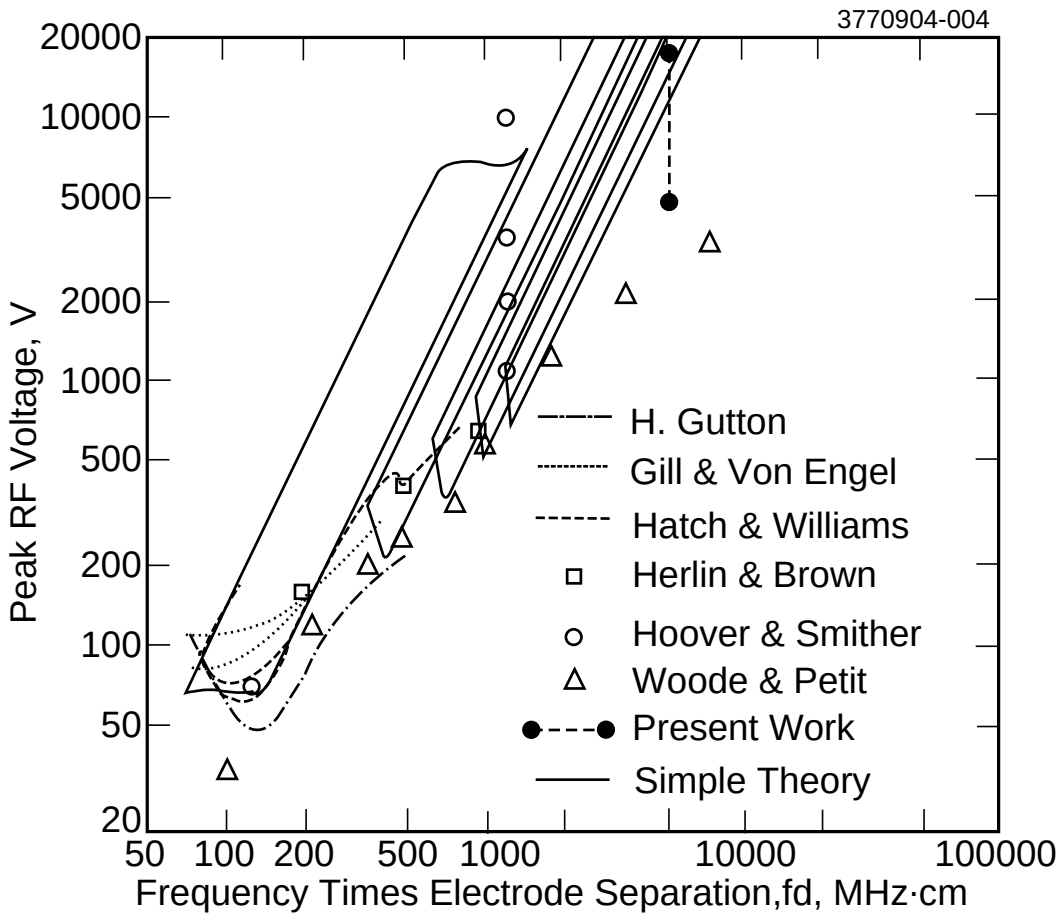

Fig. 1. Hatch diagram reproduced from Ref. [6]. Theoretical curves show the first five multipacting zones, the order being 1, 3, 5, 7, 9 from left to right. Most experimental data are pertaining to parallel-plate geometry, except Hoover & Smither (empty circle) for a cylindrical RF cavity and Woode & Petit (empty triangle) for rectangular waveguides [8]. The parameter range of the present work is also shown.

the hardness of multipacting barriers. In addition, the parallel-plate model, on which the Hatch diagram is based, is not able to account for the the effect of the RF magnetic field which presents inherently inside the waveguide operated in the propagating TE_{10} mode.

The understanding of multipacting in a rectangular waveguide has been advanced recently by 3-D numerical studies [3][9]. In these simulations, both the electric and magnetic components of the RF field are considered. In contrast to the "constant k" (k being the ratio between the impact and emission velocity) model adopted by the aforementioned theoretical work, the more realistic "constant emission velocity" model is implemented in simulation studies. It is assumed that secondary electrons are emitted normal to the surface with a fixed initial energy of 2-5 eV. The trajectory and velocity of an emitted electron are calculated by integrating its equation of motion. The kinetic energy of electrons upon impact with a surface is used to determine the secondary

electron yield (SEY). Curves of the SEY dependence on the impact energy for commonly used practical materials can be found in [10][11]. Trajectory calculations are performed for a large number of electrons emitted with different initial locations and RF phase angles. The algorithm identifies multipacting when many electrons with favorable phase angles survive 20-30 generations of impact. In addition, the SEY has to meet certain criterion so that the number of electrons has a net gain. A multipacting band map, or the intensity of multipacting barriers as a function of the RF power, is constructed when the above mentioned procedure is repeated for many power levels. A typical multipacting band map generated by this algorithm represents discrete multipacting barriers, each corresponding to a resonant condition of a specific order and a stable phase angle range. Simulation studies confirmed the existence of two-sided higher order multipacting in the waveguide coupler of the superconducting RF system for CESR [12]. Further more, the magnetic bias method was proposed for multipacting suppression in a rectangular waveguide, which was shortly confirmed by experiments [13].

The theoretical treatments and numerical simulations of the two-sided multipacting phenomenon have been successful. However, one must realize that RF breakdown originated from multipacting can not be fully understood without including the interaction between multipacting electrons and desorbed gas molecules, coming from either thermal desorption or electron stimulated desorption (ESD). As will be shown in this paper, the ESD effect plays a critical role in the process of multipacting induced breakdown. Although in principle this effect can be studied analytically or numerically, very limited work has been so done. An experimental study of this effect appears to be necessary. The purpose of this paper is to present experimental studies of multipacting induced breakdown in rectangular waveguide geometry. Multipacting characteristics, such as the band structure, spatial distribution and the saturation effect, are presented in Sec. 3.1. In what follows, Sec. 3.2 deals with the electron energy spectrum. The effect of ESD is discussed in Sec. 3.3. All data presented in this paper, except otherwise specified explicitly, are pertaining to measurements in traveling wave mode.

2 Experimental setup and diagnostics

Experiments were performed using two different waveguides. A detailed description of the experimental setup with the first waveguide has already been published in Ref. [13]. For completeness, a brief description is given in this paper. The RF power was provided by a klystron with a maximum power output of 600 kW in CW mode. Experiments were conducted in the pulsed mode because of the power limitation of the water load and of the vacuum barriers in the waveguide. The RF pulse length is typically 2 ms and the rep-

etition rate is 10 Hz. The cross-section of test waveguides has a dimension of 457 mm×102 mm. The waveguide length is 610 mm, which is chosen to be longer than a half of the guided wavelength. The vacuum inside the waveguide space was maintained by a 50 l/s turbo molecular pump attached to the narrow wall of the waveguide through a slotted hole. A baseline pressure of 5×10^{-6} torr was achieved before the RF was applied.

Electron pick-up probes of antenna type were mounted at various locations on the broad wall and narrow wall of the waveguide. Initially, electron pick-up probes were populated along the center line of the broad wall, where the RF electric field is maximum. The second waveguide had added probes across the broad dimension, allowing to resolve the horizontal distribution of the multipacting current intensity. More details about this set-up can be found in [14]. All probes were positively biased with 24 V batteries to avoid secondary electron emission from the probes. A photo multiplier tube (PMT) mounted on the narrow wall was used to monitor light activities inside the waveguide space. A cold cathode gauge, also mounted on the narrow wall, was used to measure the waveguide vacuum. Fig.2 shows locations of the electron pick-up probes, PMT and cold cathode gauge. The RF system has a protective interlock system which shuts off the RF power in case the PMT light or the waveguide vacuum pressure exceeds the preset threshold. The RF control system recovers automatically the RF after the occurrence of a trip.

The electron energy spectrum was measured with an electron energy analyzer (EEA) which utilizes the retarding field method [15]. As sketched in Fig. 3, the EEA consists of two mesh electrodes and the Faraday cup. The first mesh electrode is grounded to the waveguide body. The second mesh electrode is biased with a variable negative voltage, providing the retarding potential. To suppress secondary electron emission due to the electrons being detected, the Faraday cup features a cone-shaped inner surface. Further suppression was provided by biasing the Faraday cup with a 24 V battery.

3 Experimental results

3.1 Multipacting characteristics

3.1.1 Multipacting band structure

We refer to the multipacting band structure as the RF power dependence of the multipacting current intensity. It depends strongly on the power history of a waveguide. When the RF power was initially applied, multipacting started usually at a low power of 30-70 kW. The probe currents were also accom-

panied by light emission from the waveguide space, whitish-blue in color, as observed through the Mylar window and the view port. The intensity of the light as monitored by the PMT grew rapidly and soon exceeded the interlocking threshold. Then a trip occurred and the RF was shut off. By bringing the RF back repeatedly and allowing the multipacting to "process", it was eventually possible to keep the RF power static. However, raising the power to a higher level by a small step would readily be interrupted by the interlocking PMT light and it was necessary to process again at the new power level. The needed processing time for each power step varies. Nevertheless, it was possible to bring the pulsed RF power to the highest level of 550 kW in the traveling wave mode. The multipacting measurements were typically performed by scanning the RF power downward after the completion of RF processing. The post-processing multipacting is characterized with a fairly stable electron current and there is no observable light emission coming from the waveguide space. Fig. 4(a) shows a typical multipacting band obtained over the course of RF processing. The multipacting band after RF processing is shown in Fig. 4(b). It can be seen that RF processing virtually eliminates the multipacting in the lower power range but has little effect in the higher power range.

The numerically calculated multipacting band is shown in Fig. 4(c).Each peak represents a multipacting barrier of a specific order. The electron impact energy is also shown next to the corresponding peak. The discrete multipacting band structure predicted by numerical simulations is in sharp contrast with those obtained by our experiments, in which multipacting peaks are suppressed significantly. Nevertheless, a qualitative agreement between the calculated and measured multipacting bands still exists with regard to the barrier position and the number of barriers. The current spikes recorded below 200 kW during RF processing (Fig. 4(a)) represent an even better agreement, despite a poor measurement resolution in this stage because of the fleeting nature of multipacting during processing.

The light emission phenomenon observed during the processing period is suggestive of ionization discharge of some kind of gas molecules. As will be shown later, gaseous ionization discharge is the consequence of the developing multipacting in the waveguide and the very direct cause for RF breakdown. This effect will be discussed in greater details in Sec. 4.4. It should be pointed out that, for the discussion of multipacting characteristics, we refer only to post-processed waveguides in which "clean" multipacting develops with an unambiguously defined current.

Multipacting bands for standing wave and partial reflection wave modes were also obtained and the result has been published previously [13]. The multipacting onset power (for after processing) decreases to 90 kW for the standing wave mode, as compared to 180 kW for the traveling wave mode. The on-

set power for a partial reflection mode falls in between 90 and 180 kW and amounts to 120 kW for a 16.6% reflection ratio. It is also noticed that the peak of multipacting barriers becomes progressively less distinctive as the reflection ratio is increased.

3.1.2 Spatial distribution

Measurements with the first waveguide set-up showed unexpectedly a large current near the narrow wall surface. Fig. 5 shows the current detected by the narrow wall probe P1 as well as those by the broad wall probes P2-P4 when a traveling wave passes through the processed waveguide. It is noted that the narrow wall current has nearly a monotonic dependence on the forward power, in contrast to the broad wall currents which have structures representing multipacting bands[2]. The longitudinal distribution of the multipacting current is obtained by comparing curves (Fig. 5) of P2-P4, which are distributed on the center line of the broad wall with a probe distance of 5.6 cm as shown in Fig. 2. It is seen that the multipacting current has a reasonably uniform longitudinal distribution with some minor difference attributable to the variation of the waveguide height due to deflection of the broad wall under the atmospheric pressure. The maximum deflection amounts to 20% of the height of the earlier waveguides.

The observation of a large narrow wall current motivated us to add more pick-up probes across the broad wall of the second waveguide so as to measure the horizontal distribution of the multipacting current [14]. Five probes are uniformly distributed across the broad wall, probe P3 being at the center. The other probes form two pairs, both symmetric about P3. The inner and outer pair consists of P6 and P7 and P5 and P8, respectively. The result is shown in Fig. 6 and a symmetric horizontal distribution of the multipacting current is evident. Above 280 kW, the multipacting current has a minimum at the center of the broad wall where the RF electric field is maximum. It increases with the distance from the center of the broad wall and reaches maxima at the narrow walls.

3.1.3 Saturation

Given the resonant nature of multipacting, ideally the number of electrons should grow exponentially with time. For the two-sided higher order multipacting (N>9) discussed in this paper, it is estimated that a multiplication factor on the order of 1 billion would be reached in less than 1 μs. This type of fast electron avalanche was not however observed during the experiments.

[2] It should be noted that the curve of the P1 current has recognizable kinks at power levels corresponding to multipacting peaks.

Instead, as shown in Fig. 7, a saturated multipacting current was detected (for a processed waveguide) on the time scale of 10^{-3} s. The current density was measured to be less than 0.1 mA/cm^2. During the processing period, the multipacting current sometimes exhibited noisy oscillations with a peak current density as high as 1 mA/cm^2; but the envelope of the oscillation was still rather static. It is noticed that no reflected power was measured in either case, suggesting that a saturated multipacting current presents negligible perturbation of the waveguide impedance.

The classical picture of the Nth order multipacting is that there are N sheets of electron clouds bouncing back and forth between the two broad walls [16]. During the initial multipacting build-up period, the sheets are thin and the boundary of the sheets are determined by the limiting phase angles within which multipacting resonance is stable. Because the charge density in a sheet increases rapidly as multipacting develops, the space charge effect soon becomes important. Electrons at the boundary of the sheets receive a repulsive force and are dispersed out of phase with the multipacting resonance. The observed saturation effect may be explained by electron loss due to space charge induced phase dispersion. As will be shown in Sec. 4.4, lost electrons with a 90° phase dispersion have great importance in the later stage of multipacting induced breakdown. Another possible saturation mechanism involves space charge limited emission [17].

3.2 Electron energy spectrum

Electron energy spectra measured by the EEA installed behind a 18 mm diameter hole on the broad wall (Fig. 2) are shown in Fig. 8 for various forward power levels in traveling wave mode. All measurements were performed with processed waveguides. The abscissa is the retarding voltage and the ordinate is the Faraday cup signal due to electrons capable of overcoming the retarding field. The Faraday cup signal decreases rapidly with the retarding potential. The maximum electron energy, being determined by the end-point potential in a spectrum, is in the range of 100-1000 eV for the interested RF power range of 50-500 kW.

Fig. 9 shows a typical differentiated energy spectrum, which is obtained for a 250 kW forward power in traveling wave mode. The end-point energy is recognized at 475 eV where the signal intensity starts to rise rapidly with a decreasing electron energy. It is also evident that there exist two groups of electrons, divided approximately at 50 eV. The dividing-point energy is found to be rather insensitive to the RF power and is in the range of 30-100 eV for the interested RF power range. In contrast, the end-point energy has a linear dependence on the forward power.

3.3 Electron stimulated gas desorption

A close correlation between the multipacting current and the waveguide vacuum was observed during the processing period. This is shown in Fig. 10. The RF power was held constant at 150 kW in traveling wave mode and was pulsed at 10 Hz for a pulse width of 2 ms. Both the waveguide pressure and probe current increased with time when the RF was initially applied. The intensity of light inside the waveguide space, as detected by the PMT, increased also until the RF was tripped off by a large PMT signal exceeding the pre-set threshold. The waveguide pressure was reduced during the RF recovery period due to evacuation by the turbo molecular pump. The RF, when it was restored, led to similar increases in waveguide pressure and PMT light trips. The trip-recovery cycle usually repeated itself several times and finally a stable RF could be maintained without interruption. After a certain processing time was reached, the waveguide pressure started to decrease monotonically, despite the existence of a significant multipacting current. In this quasi-equilibrium state, no light emission was observable. For the case shown in Fig. 10, the pressure started to drop when an accumulated processing time of 25 s was reached. This corresponds to an electron irradiation dose in the range of 0.3-3$\times 10^{15}$ electron/cm^2 over the waveguide surface in the high electric field region [3] . The multipacting current decreased along with the waveguide pressure. However, the decrease in the current was much slower than that in the pressure. For the case in Fig. 10, the current and pressure are decreased by 8% and 60% respectively when an accumulated processing time of 100 s is reached. After the waveguide was thoroughly processed up to the maximum power, the waveguide vacuum was much less affected by the RF power. In the high power range, the waveguide pressure was somewhat higher due to an elevated temperature of the waveguide surface caused by RF heating; but in the low power range, it was possible to achieve a vacuum level comparable to the baseline vacuum obtained before the RF was applied. The final multipacting current was however rather static.

In the presence of both RF and multipacting, the waveguide pressure increase arises from two mechanisms: thermal desorption and ESD. The importance of thermal desorption increases as the RF power level and the time scale under consideration increase. Gas desorption stimulated by multipacting electrons which occurs simultaneously with multipacting, is the main desorbing mechanism in the low RF power range. This is demonstrated by the reaction of the waveguide vacuum to a multipacting suppression solenoid magnetic field, as shown in Fig. 8 of an earlier publication of our studies [13]. The waveguide pressure remains unchanged when the RF (80 kW) is applied in the absence

[3] The effective electron irradiation time is reduced to 0.5 s due to the 2% RF duty factor; The multipacting current density is in the range of 0.1-1 mA/cm^2.

of multipacting, which is suppressed by a bias magnetic field. However, reactivating multipacting by removing the bias field results in an immediate pressure rise.

The ESD effect due to multipacting electrons is corroborated by gas species analysis performed with operating waveguide couplers (which are cryogenically cooled for a temperature range of 4.5-300 K) in the CESR superconducting RF system. Fig. 11(a) shows the RGA (residual gas analyzer) spectrum for a zero RF power. It indicates typical residual gas species. Fig. 11(b) shows the spectrum for a forward RF power of $\sim$ 90 kW, supporting a 250 mA storage ring current. By comparing Fig. 11(a) and (b), it is evident that the waveguide pressure and the gas species are not much affected by the sole presence of the RF. At a slightly (about 5%) higher RF power, multipacting emerged, as indicated by an increased level of PMT light, causing RF trips. New species were recorded and the waveguide pressure increased by an order of magnitude, as shown in Fig. 11(c). Because of the smallness of the increase in the RF power, thermal desorption is insufficient to account for these changes and ESD must be responsible. Under various conditions, other species have also been observed, including notably hydrogen, water vapor, carbon monoxide and nitrogen.

4 Discussion

4.1 Broadening and overlapping of multipacting barriers

It is well known that emitted secondary electrons have a spectrum of energies. The energy distribution of secondary electrons have been conventionally divided into three regions representing true secondary electrons, inelastically scattered primary electrons, and elastically scattered primary electrons [18]. Numerical simulations have instead adopted a constant emission velocity model and predicted discrete multipacting bands. Apparently, this is a simplified picture. The continuous multipacting band structure revealed by our experiments may be, at least partially, explained by the mode broadening effect due to the spread in the velocity of secondary electrons. This has been investigated by using a Mathcad program, exploiting formulas based on Vaughan's work [16] with some necessary corrections [4]. We have shown that, by allowing a spread of 0-10 eV in the emission energy, the classical multipacting modes are broadened significantly and some modes become even overlapped. One is

[4] Equation (6a) in Ref. [16] should be corrected to $V_i = \frac{2V_{rf}\cos^2\alpha}{N\pi\cos\alpha+2\sin\alpha}$, according to derivations made by present authors (RGC & RLG).

reminded that the secondary electrons have an intrinsic energy distribution, typically in the range of 0-20 eV.

Recent simulations using the MAGIC code have shown that many of the electrons that are generated outside the stable phase range remain in the waveguide space and may, after several impacts with the wall (either scattered elastically or led to true secondary electron generation), rejoin a phase range where stable multipacting builds up according to the classical mechanism [14]. This leads to cross-talk between the overlapped modes and further contribute to broadening and merging of the multipacting barriers. The effect of elastical scattering of low energy electrons have been recently discussed in greater details in [19]. It should also be mentioned that the broadening of multipacting barriers may yet be brought about by a hybrid resonant mode mechanism coupled with the spread of initial velocity of secondary electrons [20].

4.2 Spatial distribution of multipacting current

The measured longitudinal distribution of the multipacting current is well within expectations. But the measured current distribution in the horizontal direction is a surprise, because numerical simulations predicted that multipacting is unstable outside the vertical symmetry plane of the waveguide. The observation of a large current at the narrow wall is another surprise and for two reasons it can not be explained by multipacting. Firstly, the narrow wall current depends on the RF power nearly monotonically, suggesting its origin from some non-resonant process. Secondly, numerical simulations suggested that electrons emitted from the narrow wall rarely develop into resonant type trajectories that can lead to multipacting. In this section, the observed horizontal distribution is accounted for by a seeded non-resonant multipacting mechanism.

The traveling wave electro-magnetic fields of the propagating TE_{10} mode in a rectangular waveguide are illustrated in Fig. 2. When denoting the waveguide broad dimension as a and narrow dimension as b, it can be described by

$$\begin{cases} E_y = E_0 \sin(\frac{\pi x}{a}) \cos(\omega t - kz), \\ B_x = \frac{-k}{\omega} E_0 \sin(\frac{\pi x}{a}) \cos(\omega t - kz), \\ B_z = \frac{-\pi}{\omega a} E_0 \cos(\frac{\pi x}{a}) \sin(\omega t - kz), \end{cases} \tag{1}$$

where E_0 is the maximum electric field of the forward wave, $\omega = 2\pi f$ is the angular frequency of the field, $k = \sqrt{\omega^2 \mu\epsilon - (\frac{\pi}{a})^2}$ is the propagation constant, t is time. E_0 is related to the forward RF power (P_f) through $P_f = \frac{E_0^2 abk}{4\omega\mu}$.

Driven by the RF electric field E_y, multipacting electrons have a dominant vertical velocity component v_y. Numerical simulations based on the constant emission velocity model reveal that resonant type multipacting can only happen in the vertical symmetry plane at $x = a/2$ (cut plane 2 in Fig. 2). The trajectory of multipacting electrons in this plane has a major oscillatory movement in y direction superimposed with a drifting movement in z direction because of the Lorentz force of ev_yB_x. The drift velocity is about 1% of the time averaged v_y and a drifting distance on the order of a few cm is achieved after 30 successive impacts. It is evident that as long as the waveguide has a length of more than a few cm, resonant type electron multiplication will sustain in the wave propagation direction (given that the SEY of the waveguide is larger than unity).

Electrons initiated with an offset with respect to the central line of the broad wall experience a horizontal Lorentz force of ev_yB_z. As a result, the electron trajectory drifts away from the vertical symmetry plane and the impact point has a larger offset with respect to the central line of the broad wall. The trajectory of the next generation secondary electrons continues to drift away from the vertical symmetry plane, because both the velocity and the magnetic field have flipped theirs signs upon secondary emission. It has been shown that electrons originated with a few cm offset from the central line of the broad wall can only impact the broad walls several times and ultimately end up impacting the narrow wall [9]. Since the electric field near the narrow wall is very small, further multiplication is not allowed.

For the above mentioned reasons, we attribute the current detected outside the central line of the broad wall to a drifting multiplication process started from the central region. Despite its non-resonant nature, this process is sustained by continuous seeding by electrons from the central region where resonant multipacting develops. In the central region, the electron impact energy is always higher for a given RF power level and the SEY of the central surface is more efficiently reduced due to processing effect. The post-processing current is thus expected to be smaller in the central zone.At higher RF power levels, the current deficit in the central zone is further enhanced because the SEY declines with the impact energy beyond E_{max}. In the vicinity of the narrow wall, although multiplication is not allowed for lack of energy gain, low energy electrons can nevertheless persist because of high probability of elastic scattering off the wall leading to the sustained cloud. Simulations using the MAGIC code have shown that a cloud of low energy electrons forms near the narrow wall surface [14].

4.3 Electron energies

In Fig. 12, the measured end-point energy is compared to the electron impact energy predicted by numerical simulations and analytical analyses. The numerical bands obtained with the code Xing are well separated from each other, as already shown in Fig. 4(c). The bandwidth, as bounded by boundary power levels indicated in Fig. 12, of each band is nominally less than 28 kW. The analytical bands, according to the constant emission velocity (2 eV is taken here) model, are also separated and the bandwidth is determined by the limiting phase angles [16]. The lower boundary corresponds to the minimum RF power needed to sustain the multipacting and is determined by the limiting phase angle of $arctan(2/N\pi)$ [16][21]. The upper boundary is determined by the second limiting phase angle of $-arctan(2/N\pi)$ [21][22]. Here the initial velocity dependent term in the second limiting phase has been neglected because of the smallness of the initial velocity and the largeness of the order of the multipacting. It turns out that the limiting phase angles stay within a rather narrow range near the zero-crossing phase angle of the RF field. Consequently, the analytical bandwidth is exceedingly narrow. Measurements of the impact energy were performed not only at power levels corresponding to classical bands but also at power levels outside these bands. This becomes necessary when one realizes that the measured multipacting band is continuous (Sec. 3.1.1). A good agreement between the measured end-point energy and the predicted energy is evident, for example at 90 kW and 250 kW.

It is not surprising to notice that the end-point energy measured at power levels outside the classical bands follows a linear power dependence virtually identical to that inside the classical bands. The linear dependence of the impact energy on the RF power appears to be valid over the entire power range. Fig. 12 also includes a solid line, representing the curve derived from a naive multipacting model. In this model, the RF magnetic field and the initial velocity of the secondary electrons have been both neglected and secondaries are assumed to emit exactly when the RF electric field crosses zero. Such an arrangement allows the model to predict the impact energy E_i without internal parameters such as the resonance phase angles or the emission energy. Instead, E_i can be totally determined by the waveguide dimensions and the RF frequency and power (in traveling wave mode),

$$E_i[eV] = \frac{2e\mu_0}{m\pi^2}\frac{1}{fb}\frac{1}{\sqrt{(\frac{a}{\lambda})^2 - \frac{1}{4}}}P_F, \tag{2}$$

where e is the electron charge, m the electron mass, μ_0 the permeability of vacuum, f the RF frequency, b the waveguide narrow dimension, a the waveguide broad dimension, λ the free space wavelength, and P_F the RF power. All

quantities are in SI units except the impact energy, which is in eV. Eq. 2 agrees with the experimental data reasonably well and may be conveniently used to determine if a waveguide is susceptible to multipacting by comparing E_i with the cross-over impact energy of the SEY curve of the waveguide material. Eq. 2 is verified for higher order (N>9) multipacting under the present study. Its validity for lower order multipacting (which occurs at higher power) should be further tested. The order of multipacting can be estimated by

$$N = 2\lfloor p \rfloor - 1, \tag{3}$$

where

$$p = \frac{\pi m}{e\sqrt{\mu}}(fb)^{\frac{3}{2}}[(\frac{a}{\lambda})^2 - \frac{1}{4}]^{\frac{1}{4}}\frac{1}{P_F}. \tag{4}$$

Finally, it should be mentioned that 50% of electrons detected at the narrow wall have energies less than 10 eV. Only 1% have energies greater than 100 eV [14].

4.4 Gaseous ionization discharge induced by multipacting

Through the Mylar windows, which are transparent to visible light, it is observed that a breakdown event is characterized by intense whitish-blue light flashing inside the entire waveguide space. This suggests that ionization of gas molecules desorbed by multipacting electrons or by RF heating occurs. Traditional RF discharge in gases cannot properly explain the phenomenon, as it would need a pressure higher than 10^{-3} torr. In fact, the waveguide pressure rarely goes beyond 5×10^{-4} torr.

Electron energy spectrum measurements made with post-processed waveguides show that a group of slow electrons with an energy of less than 100 eV is distinctive from the higher energy electrons. The higher energy electrons are attributed to multipacting, owing to a good agreement between the endpoint energy and the impact energy predicted by the classical multipacting theory. Here we attribute low energy electrons to the dispersed (due to space charge effect) multipacting electrons that are out of phase with the multipacting resonance. For the higher order multipacting discussed in the paper, the resonant phase is nearly zero (within $\pm 5^\circ$). Analysis has shown that an electron dispersed 90° out of resonance will be captured by the RF electric field and undergoes localized oscillation movement, provided the kinetic energy of the electron is small at the moment of capture. Fig. 13(a) depicts the trajectory of a captured electron for a forward power of 250 kW. The kinetic energy of the captured electron, as shown in Fig. 13(b), varies at a frequency twice

the RF frequency and has an amplitude of about 100 eV. Both multipacting and captured electrons have sufficient kinetic energy to initiate electron impact ionization with many gas molecules [23]. For comparison, the trajectory and kinetic energy of an electron in phase with multipacting at 250 kW are shown in Fig. (c) and (d) respectively. In summary, multipacting has two consequences leading to gaseous breakdown in a rectangular waveguide: (1) an increased pressure due to stimulated gas desorption from waveguide surfaces; (2) a clod of long-life-time electrons with a kinetic energy energy capable of initiating gas ionization.

The multipacting current and waveguide pressure are the two governing parameters to warrant a breakdown event. The importance of the pressure is shown in Fig. 10. In the beginning, breakdown occurs each time the increasing waveguide pressure reaches $\sim 5 \times 10^{-5}$ torr. In the following period when the pressure is reduced, there is no more occurrence of breakdown in spite of the same level of multipacting current. On the other hand, observations made at higher RF power levels show that there is no occurrence of breakdown either when a waveguide pressure of $> 5 \times 10^{-5}$ torr is reached in the presence of an otherwise reduced multipacting current. This shows the equal importance of the multipacting current.

One should now realize that multipacting induced breakdown can be prevented either by a reduced multipacting current or by a reduced waveguide pressure. Reducing the multipacting current in a rectangular waveguide can be achieved with a number of methods, several of which have been experimentally evaluated. As shown in Sec. 3.1.1, RF processing (when sufficiently applied) is capable of eliminating the multipacting current completely in the low RF power range. The benefit of RF processing is best achieved in traveling wave mode so that the entire waveguide surface is homogeneously swept by electron bombardment [5]. The apparent drawback of the processing technique is that it requires time. One should also be warned of another limitation to the RF processing, i.e. its inability to reduce the multipacting current in the high power range. The remaining multipacting current at higher power levels in a processed waveguide can be further reduced by a factor of 2-7 with the slotted waveguide method [13]. Finally, the bias magnetic field method has the capability to completely eliminate the multipacting current in a rectangular waveguide in traveling wave mode [13]. Another classical method of

[5] For this reason, processing of the waveguide coupler in a superconducting RF system for high-current applications often needs to be performed with a beam current so that the coupler is matched with the beam-loaded cavity and a traveling wave is ensured in the coupler waveguide. The mismatch between the coupler and an empty superconducting cavity is severe because of the high unloaded quality factor of the cavity and results in a standing wave in the waveguide, in which case the surface area near minimum voltage is not effectively bombarded by multipacting electrons.

reducing the multipacting current is to coat the waveguide surface with a low SEY material. Several coatings have been experimentally evaluated recently [14]. It is stressed that the entire waveguide surface should be coated because both the broad and narrow wall are affected by multipacting. As compared to many options for reducing the multipacting current, very limited choices are available for reducing the waveguide pressure. In the context of breakdown prevention, the dynamic pressure, or the pressure in the presence of the RF and multipacting, is of the utter most importance. The only practical way of reducing the dynamic pressure is to increase the pumping speed in the vicinity of the waveguide. RF processing also has the ultimate effect of reducing the dynamic waveguide pressure but at the expense of time. Pre-baking of the waveguide is beneficial since it reduces the surface gas content and hence reduces the needed processing time.

For CW or long-pulse (>10 ms) applications at high power levels, a sufficient pumping speed is of greater importance because of the increased dynamic pressure due to gas desorption by RF heating. For a processed waveguide, although the remaining multipacting can be harmless for a short (<2 ms) pulse length at a 10 Hz repetition rate, an increased pulse length at a higher power level can again result in RF breakdown. Fig. 14 shows the development of such a breakdown event when the pulse length was increased to 10 ms from 2 ms at a forward power of 230 kW. During the beginning stage, the saturation effect limits the multipacting current and its increase is small. The current however increases rapidly afterwards and ultimately exhibits a runaway, as a result of added electrons from ionization of desorbed gases. During the final breakdown stage, some reflected power was detected at the upper-stream of the test waveguide, suggesting that the waveguide impedance is altered by the discharge. Over the course, the intensity of the light emitted from the waveguide space increased and finally reached the tripping threshold of the PMT and the RF was finally shut off by the interlock system.

Ultimately, the breakdown threshold should also be dependent on the ionization cross-section and hence the gas species and the electron energy. Although further discussion of this topic is out of the scope of this paper, we feel necessity to point out that the electron impact ionization cross-section for common gas species [6] is on the order of $1 - 3 \times 10^{-16}$ cm^2 for an electron energy of >30 eV. The present study sets the pressure threshold for multipacting induced gaseous breakdown in the range of $5 - 50 \times 10^{-5}$ torr for a multipacting current density in the range of 0.1-1 mA/cm^2.

[6] Such as H_2, CO, H_2O and N_2 etc.

5 Conclusion

Multipacting induced discharge in a rectangular waveguide has been studied experimentally. The measured multipacting band is found to have a continuous structure, in contrast with the discrete structure predicted by the constant emission velocity model. This observation is tentatively explained by the spread of initial velocities of secondary electrons. It is discovered that multipacting is active over the entire surface of the broad wall and a cloud of low energy electrons exists near the narrow wall surface. The electron energy spectrum measurements are made with the retarding field method. The end-point energy is in the range of 100-1000 eV and agrees with the impacted energy calculated by the classical resonant multipacting theory. A formula for the impact energy of higher order multipacting is derived, which can be used to determine if a rectangular waveguide is susceptible to the two-sided multipacting. This study concerns not only characteristics of multipacting but also consequential activities induced by multipacting. It is concluded that the final RF breakdown is caused by gaseous ionization discharge. Multipacting desorbs gas molecules from waveguide surfaces and provides long-life-time electrons with a kinetic energy capable of initiating electron impact ionization. Consequently, a large fraction of detected electrons have energies less than 100 eV. Multipacting induced breakdown can be prevented either by reducing the multipacting current or by reducing the dynamic waveguide pressure. It is advisable that the entire waveguide inner surface should be covered when choosing a low SEY coating for multipacting suppression. In practical situations where multipacting current reduction has limitations, sufficient pumping capacity must be provided to reduce the dynamic waveguide pressure. We believe this rule is equally applicable to coaxial lines susceptible to multipacting, as it is anticipated that the multipacting induced RF breakdown in coaxial lines is also operated by ionization discharge of desorbed gases.

6 Acknowledgment

This work is supported by the National Science Foundation and by the Diamond Light Source Company.

References

[1] J. Tückmantel, et al., Proc. of 1995 Particle Accelerator Conference and International Conference on High-Energy Accelerators, Dallas, TX, USA, 1996. P. 1642.

[2] P. Ylä-Oijala, Ph. D. Thesis, University of Helsinki (1999).

[3] R.L. Geng, H. Padamsee, Proc. of 1999 particle Accelerator Conference, New York City, USA, 1999, P. 429.

[4] G. Devanz, Phys. Rev. ST Accel. Beams 4, 012001 (2001).

[5] E.W.B. Gill, A. von Engel, Proc. R. Soc. (London) A192, (1948) 446.

[6] A.J. Hatch, H.B. Williams, Phys. Rev. 112 (1958) 681.

[7] A.J. Hatch, H.B. Williams, J. Appl. Phys. 25 (1954) 417.

[8] A. Woode, J. Petit, ESA Journal 14 (1990) 467.

[9] E. Chojnacki, Phys. Rev. ST Accel. Beams 3, 032001 (2000).

[10] V. Baglin, et al., Proc. of European Particle Accelerator Conference, Vienna, Austria, 2000, p. 217.

[11] R.E. Kirby, F.K. King, Nucl. Instr. and Meth. Phys. Res. A 469 (2001) 1.

[12] S. Belomestnykh, et al., Proc. 1999 Particle Accelerator Conference, New York City, USA, 1999, p. 980.

[13] R.L. Geng, et al., Nucl. Instr. and Meth. Phys. Res. A 508 (2003) 227.

[14] P. Goudket, Ph. D. Thesis, Lancaster University (2004).

[15] R.A. Rosenberg, K.C. Harkay, Nucl. Instr. and Meth. Phys. Res. A 453 (2000) 507.

[16] J.R.M. Vaughan, IEEE Trans. Electron Devices 35 (1988) 1172.

[17] S. Riyopoulos, Phys. Plasmas 4 (1997) 1448.

[18] H. Bruining, Physics and Applications of Secondary Electron Emission, Pergamon Press Ltd, 1954.

[19] A. Dexter, R. Seviour, P. Goudket, Proc. of the 4th International Workshop on Multipactor, Corona and Passive Intermodulation in Space RF Hardware, ESTEC, Noordwijk, The Netherlands, (2003).

[20] A. Kryazhev, et al., Phys. Plasmas 9 (2002) 4736.

[21] V.D. Shemelin, Sov. Phys. Tech. Phys. 31 (1986) 1029.

[22] V. Semenov, et al., Phys. Plasmas 8 (2001) 5034.

[23] http://physics.nist.gov/PhysRefData/Ionization/.

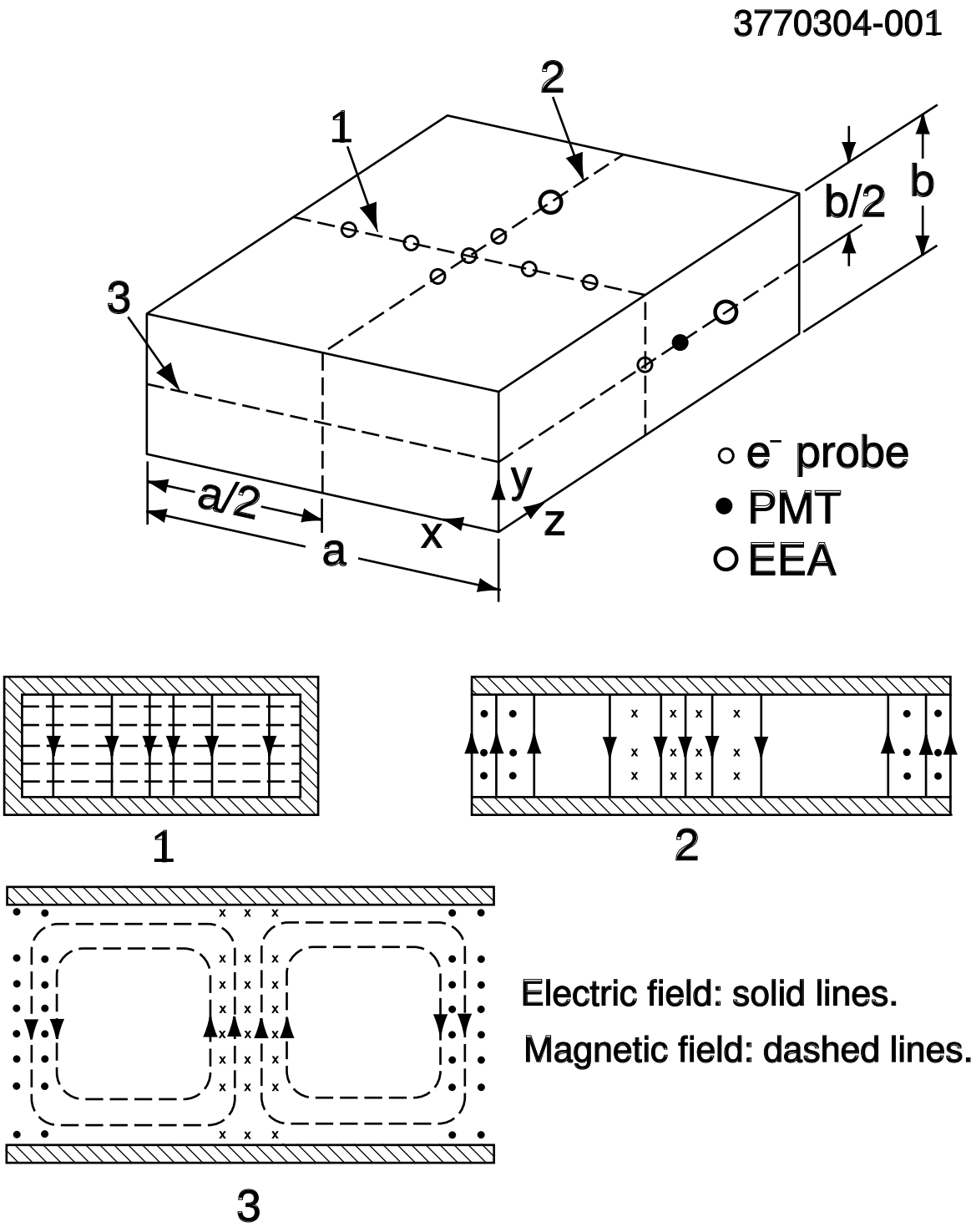

Fig. 2. Sketch of the test waveguide. The RF electric and magnetic field of the propagating TE10 mode are shown with solid and dashed lines, respectively. Locations of electron pick-up probes, PMT and electron energy analyzer (EEA) are also shown.

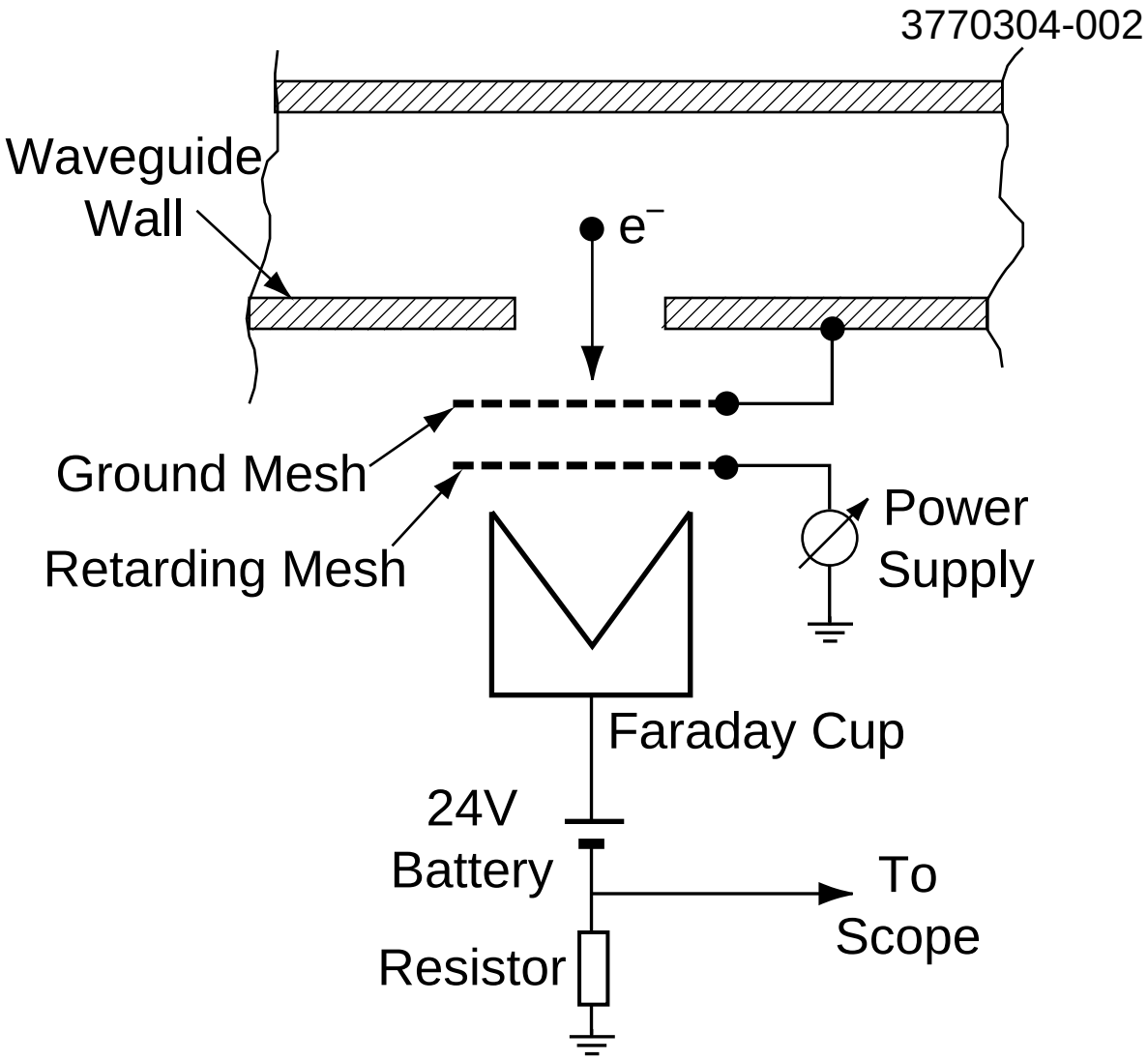

Fig. 3. Sketch of the electron energy analyzer. The ground mesh is electrically shorted with the body of the waveguide. The retarding mesh is biased with a potential in the range of 0-2000 V. The Faraday cup features a cone-shaped inner surface and is biased with a positive voltage of 24 V.

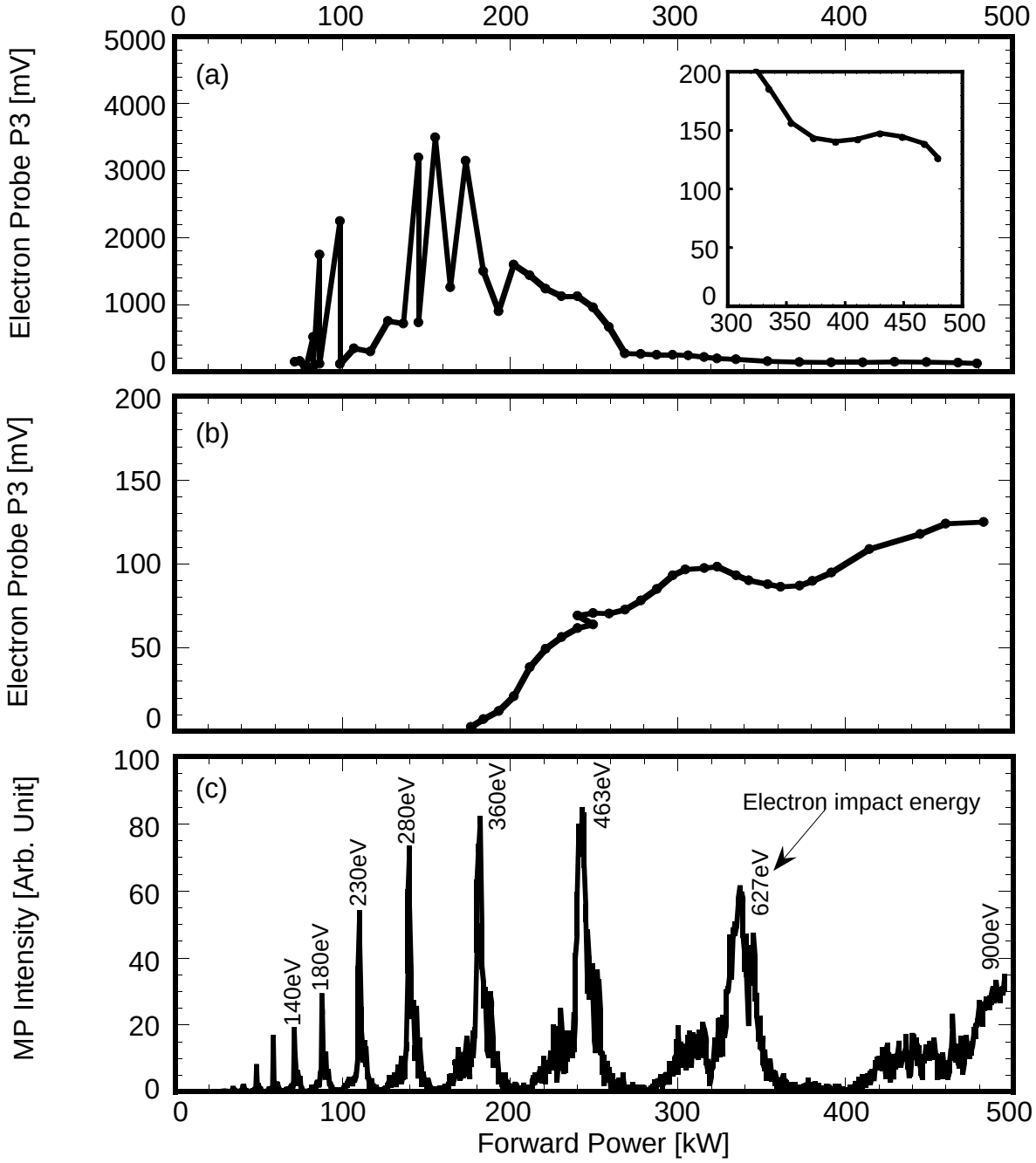

Fig. 4. Multipacting band structure in traveling wave mode. (a) Before processing. Details for the high power range is shown in the inset. (b) After processing. (c) Numerical simulation result. Electron impact energy for each calculated barriers is also shown.

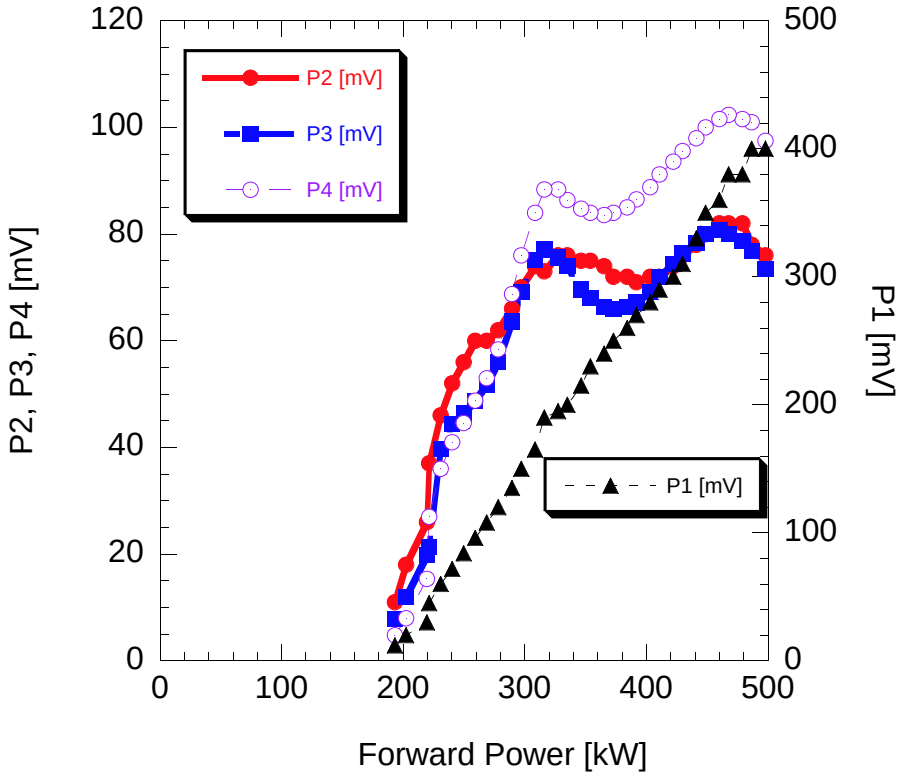

Fig. 5. Multipacting currents measured at various locations of a post-processed waveguide operated in traveling wave mode. The probe P1 is mounted at the narrow wall and probes P2-P4 at the center line of the broad wall (Fig. 2).

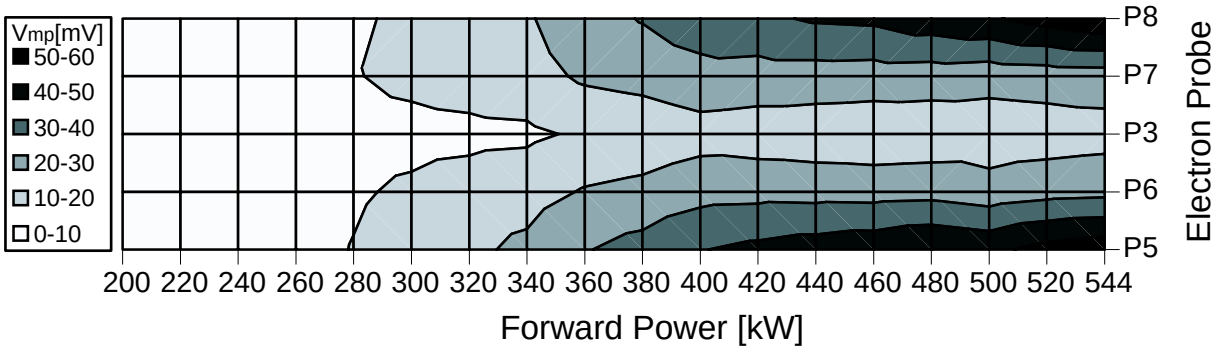

Fig. 6. Horizontal distribution of multipacting current signal (V_{mp}) of a processed waveguide operated in traveling wave mode.

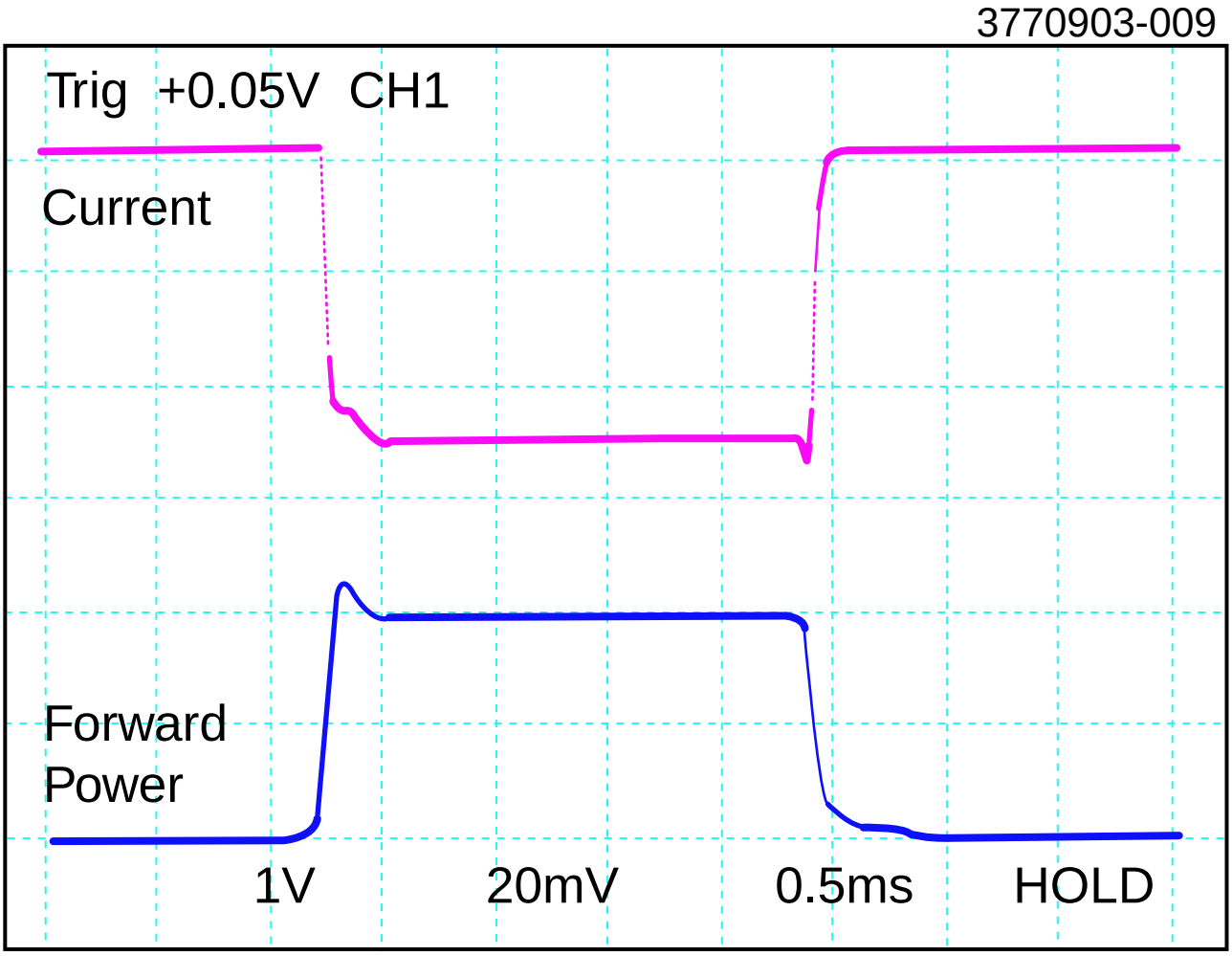

Fig. 7. Saturation effect of the multipacting current in a post-processed waveguide operated in traveling wave mode. The RF is pulsed with a 2 ms pulse length at a 10 Hz repetition rate. Lower and upper traces are the forward RF power and multipacting current, respectively.

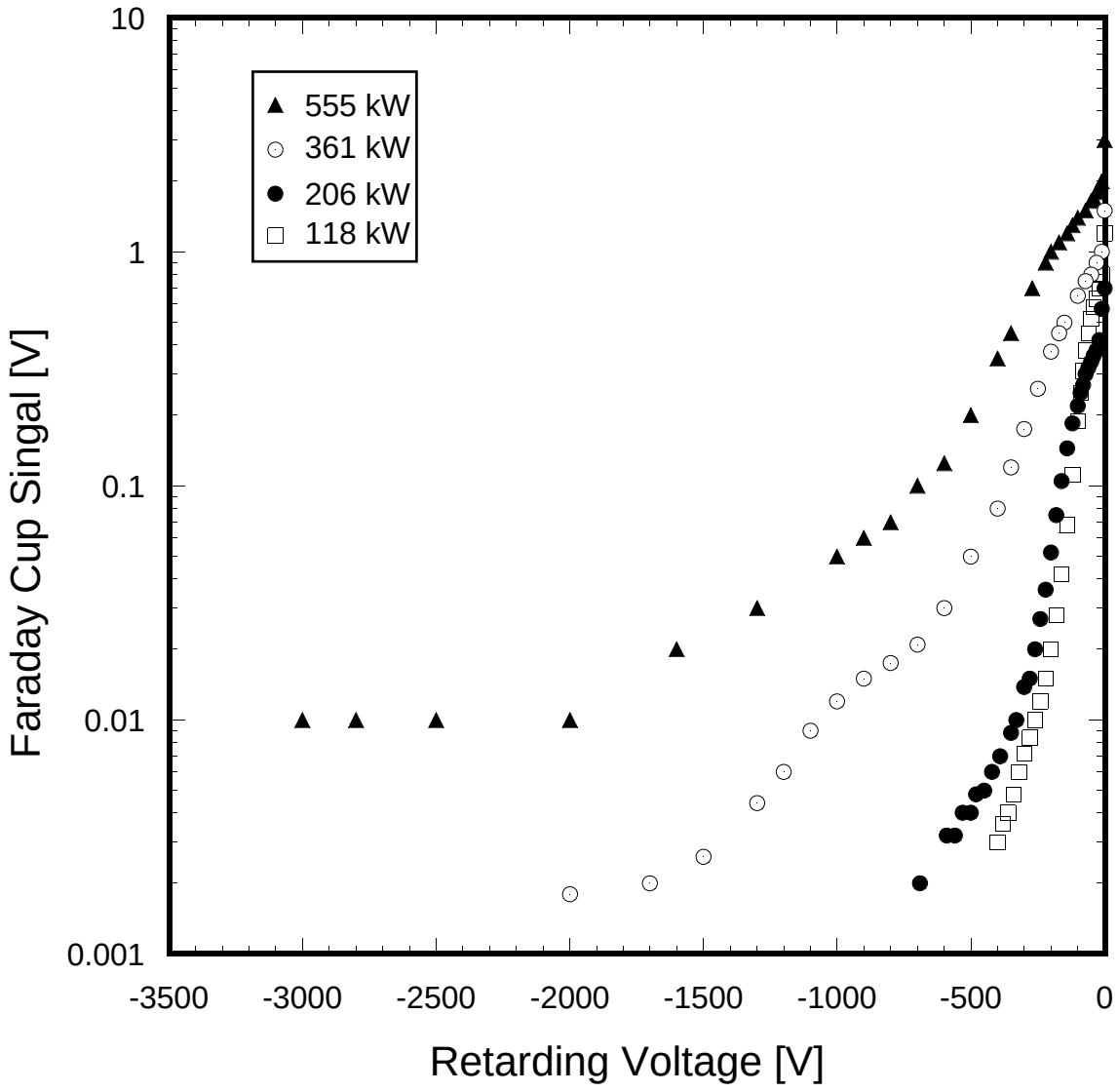

Fig. 8. Raw energy spectrum of multipacting electrons measured behind a small hole at the center of the broad wall in the traveling wave mode for various power levels.

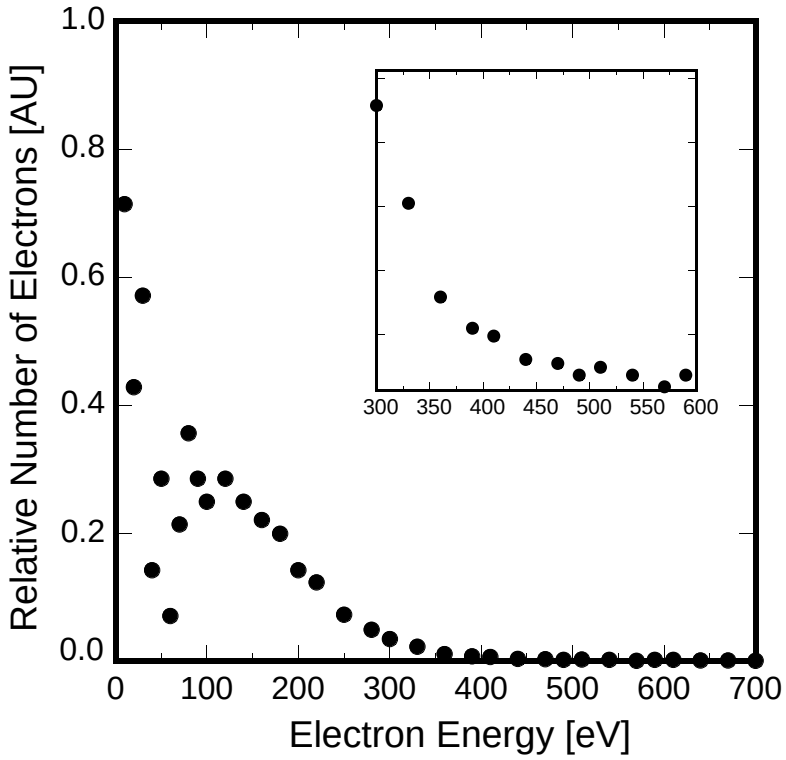

Fig. 9. Differentiated energy spectrum taken with a processed waveguide for a forward power of 250 kW in traveling wave mode. Inset shows details near the end-point energy of 475 eV.

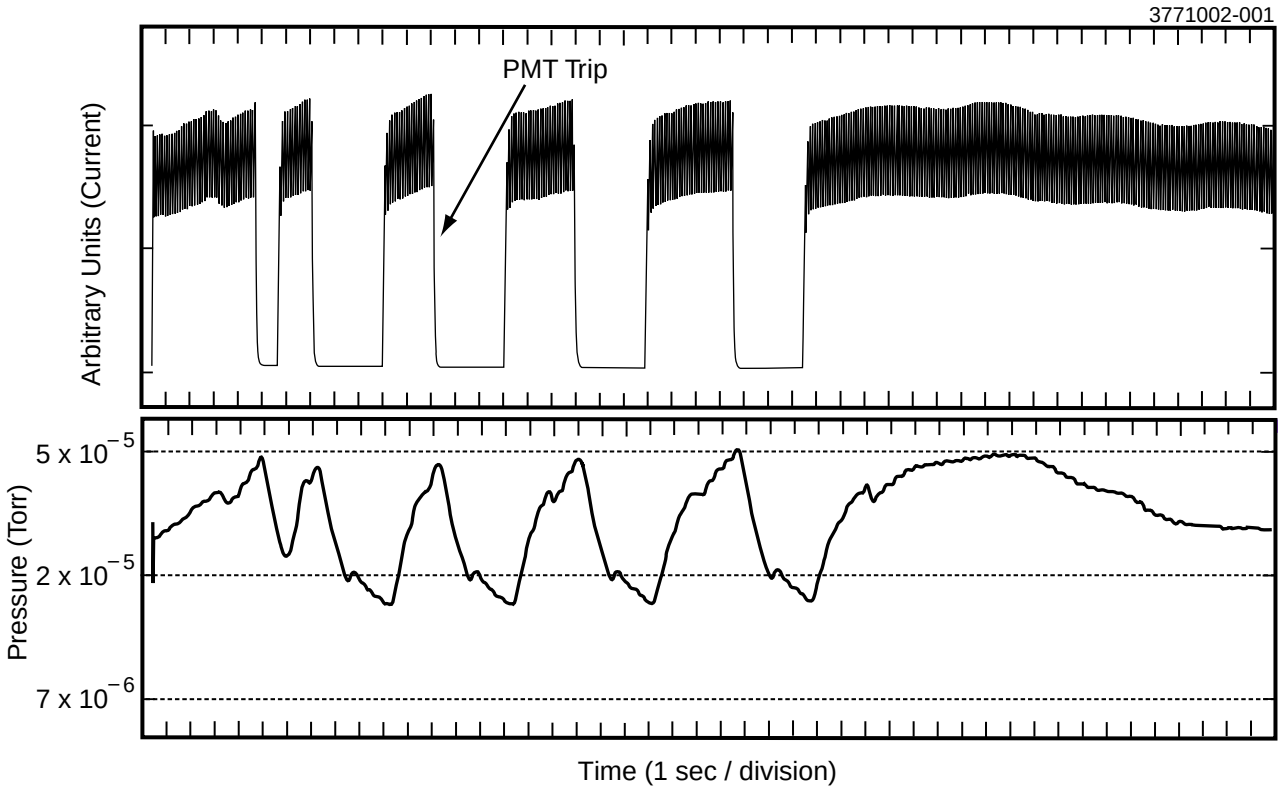

Fig. 10. Correlation between the multipacting current and the waveguide vacuum for a forward power of 150 kW in traveling wave mode. The RF is pulsed at 10 Hz for a pulse width of 2 ms. See text for explanation

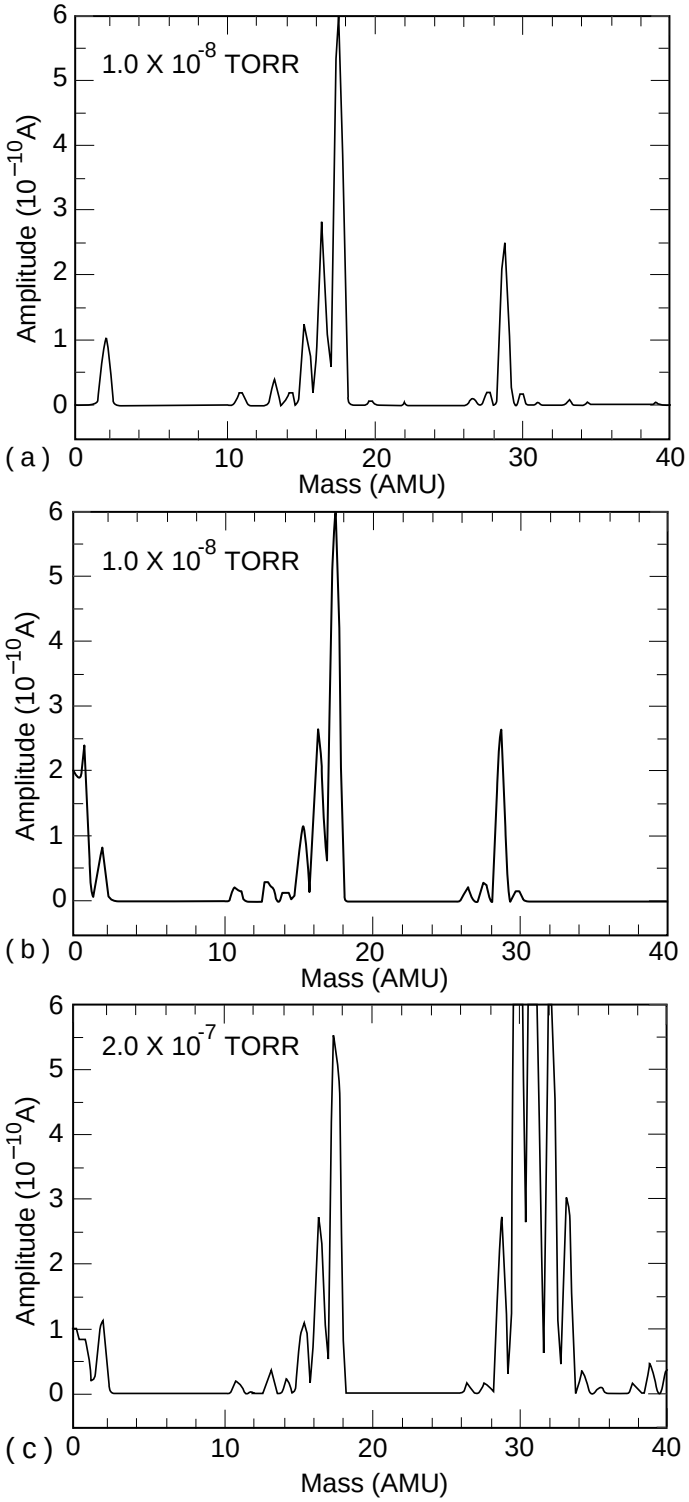

Fig. 11. RGA spectra taken with a cryogenically cooled waveguide for various conditions. (a)RF off; (b) RF on without multipacting; (c) RF on with multipacting.

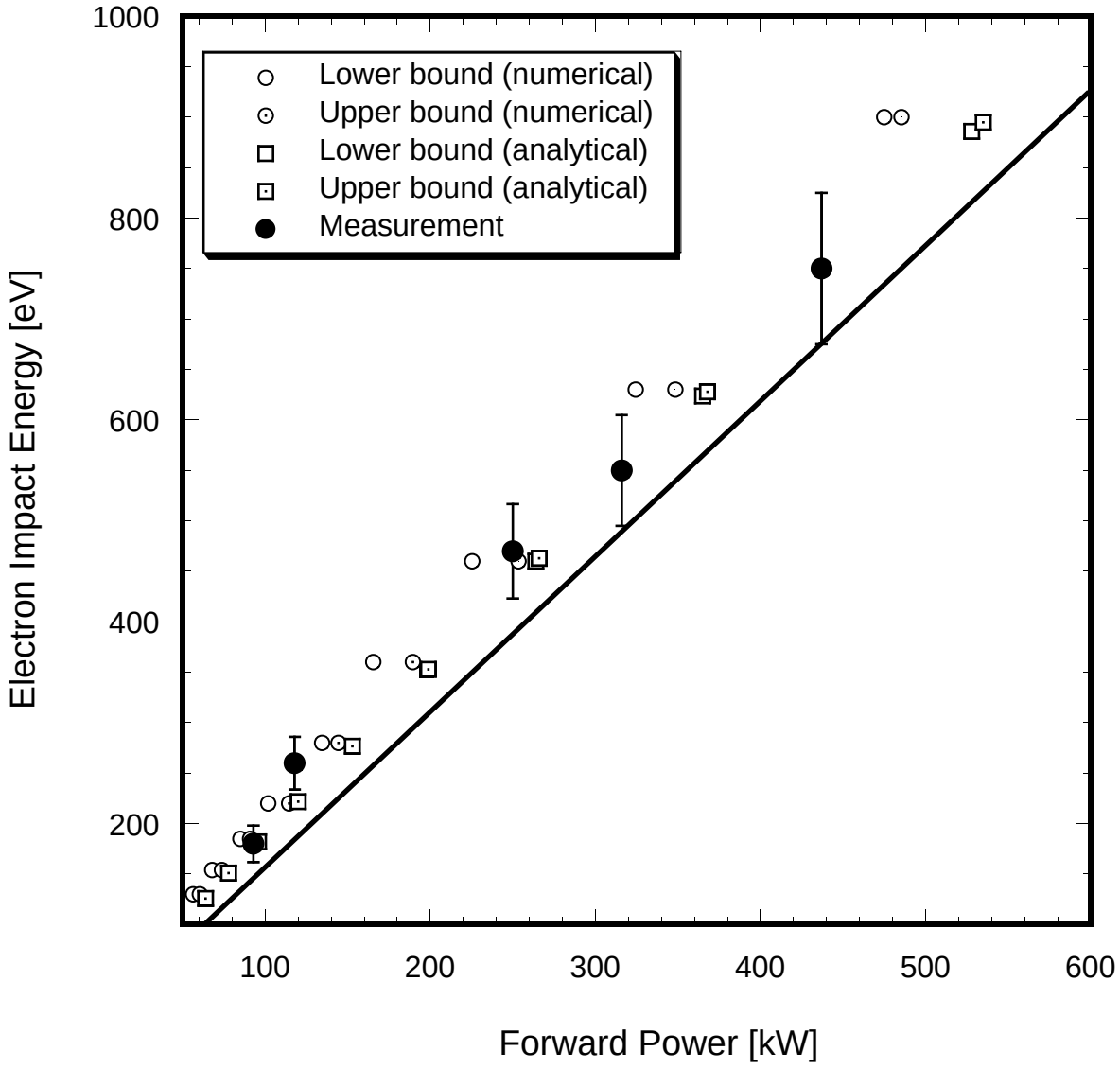

Fig. 12. Comparison of electron impact energies. Numerical results are shown in circles, analytical results in squares, and experimental results in solid circles. The solid line is due to the naive multipacting model.

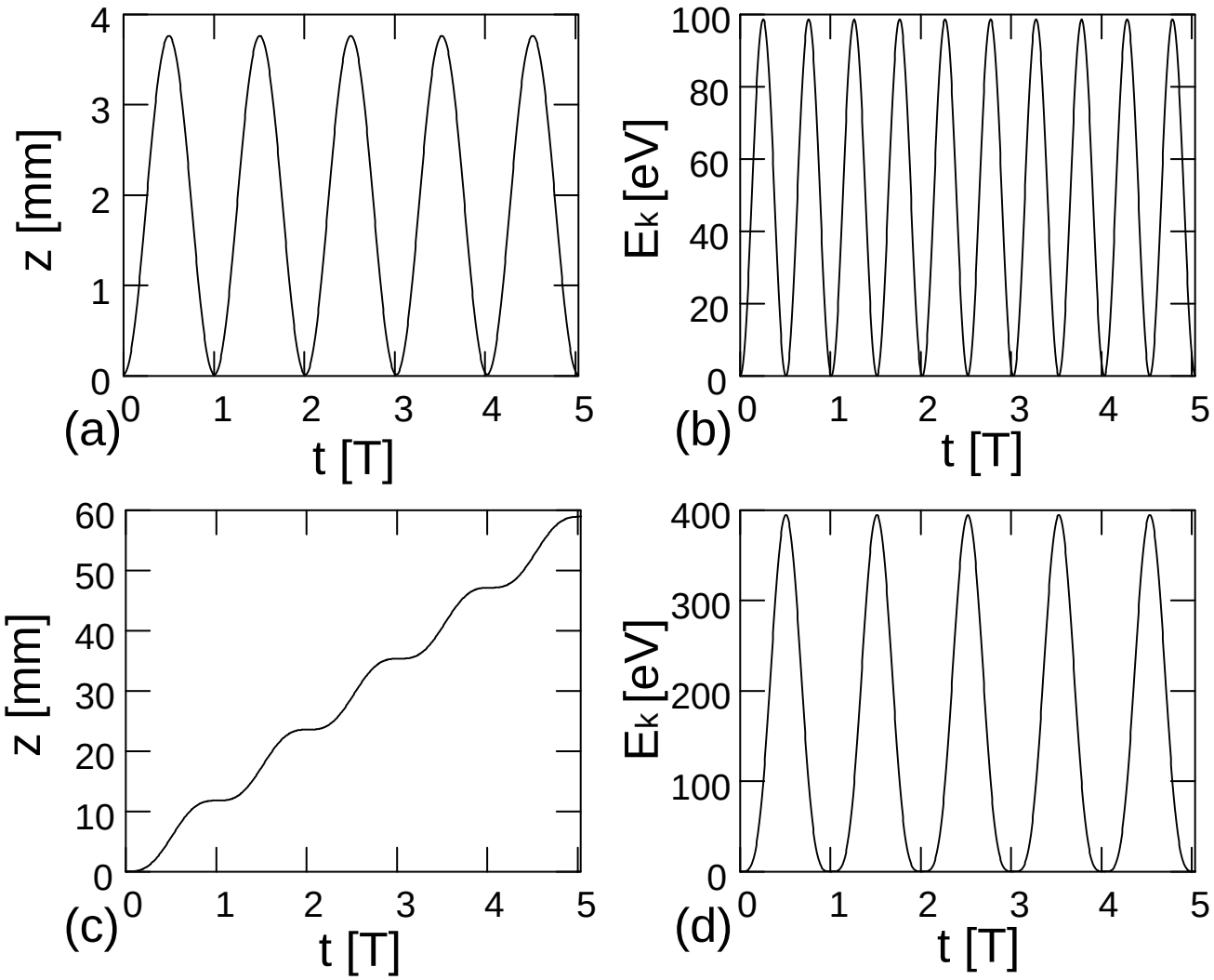

Fig. 13. Comparison of the trajectory and kinetic energy of an captured electron and an electron in phase with multipacting. The forward power is 250 kW. The abscissa is time in RF period. (a) Trajectory of the captured electron. (b) Kinetic energy of the captured electron. (c) Trajectory of the in phase electron. (d) Kinetic energy of the in phase electron.

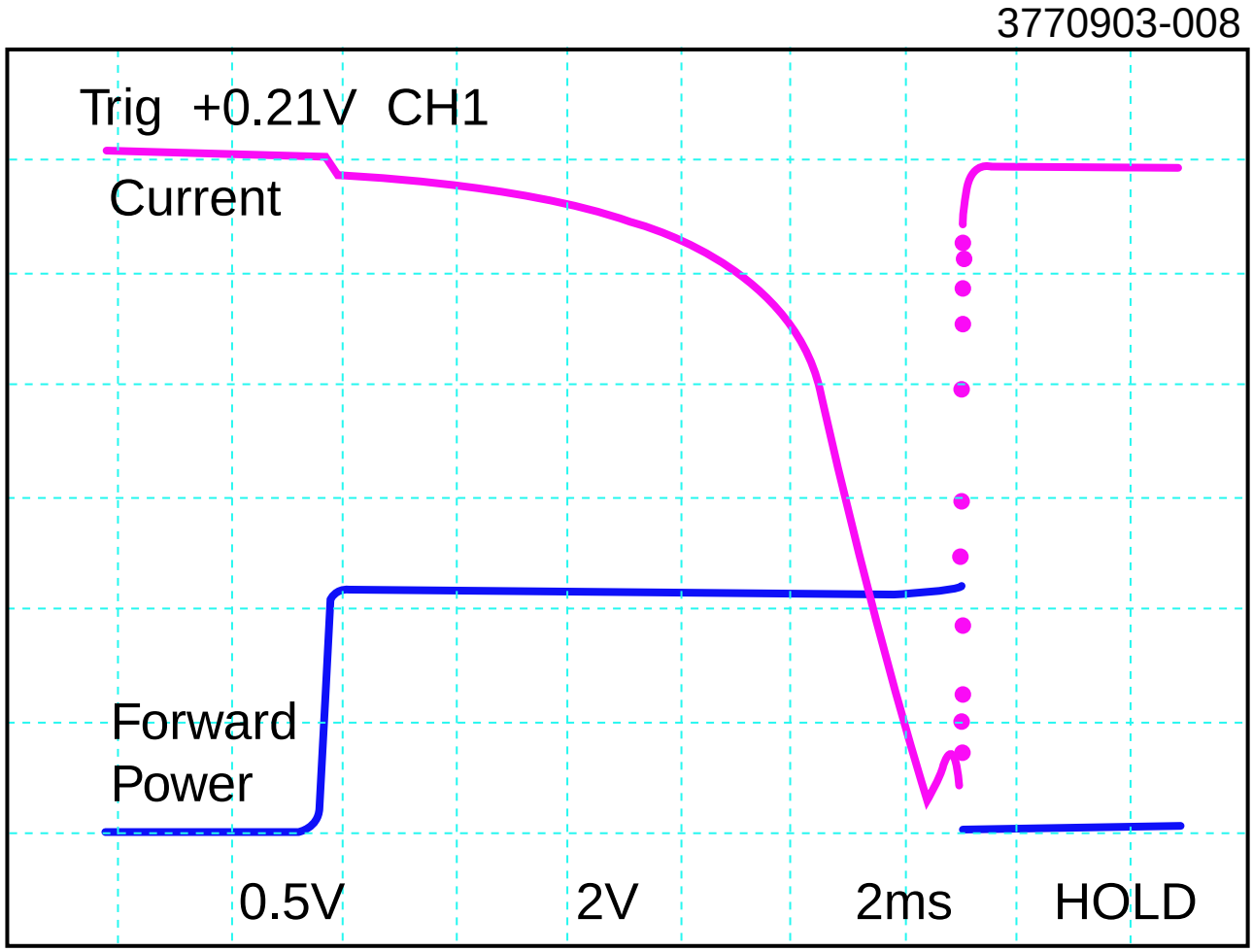

Fig. 14. Time evolution of the electron current when the RF pulse length is increased to 10 ms from 2 ms. The beginning period is dominated by a saturated multipacting current. The ending period is dominated by gaseous ionization discharge.